

**Universitat de Lleida**

Document downloaded from:

<http://hdl.handle.net/10459.1/66081>

The final publication is available at:

<https://doi.org/10.1016/j.catena.2019.03.028>

Copyright

cc-by-nc-nd, (c) Elsevier, 2019



Està subjecte a una llicència de [Reconeixement-NoComercial-SenseObraDerivada 4.0 de Creative Commons](https://creativecommons.org/licenses/by-nc-nd/4.0/)

# REMOTE SENSING MONITORING OF A COASTAL-VALLEY EARTHFLOW IN NORTHWESTERN GALICIA, SPAIN

Jesús Horacio<sup>1,2\*</sup>, Efrén Muñoz-Narciso<sup>3</sup>, Alan S. Trenhaile<sup>4</sup>, Augusto Pérez-Alberti<sup>1,2</sup>

<sup>1</sup> Department of Geography, University of Santiago de Compostela, Galicia, Spain

<sup>2</sup> Laboratory of Environmental Technology (Institute of Technological Research), University of Santiago de Compostela, Galicia, Spain

<sup>3</sup> Department of Environment and Soil Sciences (DMACS), Universitat de Lleida, Catalunya, Spain

<sup>4</sup> Department of Earth and Environmental Sciences, University of Windsor, ON, Canada

\* Corresponding author. Email: [horacio.garcia@usc.es](mailto:horacio.garcia@usc.es) Phone: (+0034) 981-563-100 (ext. 12591)

## Abstract

Historical air photographs, LiDAR, and an unmanned aerial vehicle (UAV) were used to record the movement, from 1956 to 2018, of a clay and clast earthflow in a coastal valley in northwestern Spain. Two procedures were employed. The first tracked changes, in a GIS environment, in the location of eight, easily identified objects on the surface of the deposit (large boulders, topographic lobes, and the foundations of an old hut). The second used DEMs of Difference (DoDs) based on Digital Elevation Models from a 2010 LiDAR flight and two UAV flights in 2016 and 2018 obtained by Structure from Motion-Photogrammetry techniques. While the first procedure provided estimates for earthflow movement over a 62-year period, the second produced more precise data for periods of up to 8-years. The first procedure indicated that the mean rate of movement was  $0.48 \text{ m}\cdot\text{yr}^{-1}$ , increasing from only  $0.14 \text{ m}\cdot\text{yr}^{-1}$  from 1956 to 1983 to between  $0.50$  and  $0.83 \text{ m}\cdot\text{yr}^{-1}$  from 1983 to 2018. Despite some temporal and spatial changes in direction, rates of surface movement were quite uniform on the deposit. The increase in earthflow movement after 1983 may be related to an increase in rainfall, although human activities associated with the removal of a wrecked ship from the nearshore may have been a contributing factor. The role of debuttreassing due to the wave-induced removal of lateral support from the toe of the deposit is less clear. While there was no clear relationship between wave erosion and rates of movement, coastal retreat may have triggered changes in the

29 direction and sediment flux in the toe of the deposit. This effect could have been tempered by  
30 negative feedback, however, whereby coastal erosion and increased flow activity were  
31 countered by the protection afforded by the accumulation of large, dislodged boulders on the  
32 beach. Because of this feedback, it is difficult to predict the impact of sea level rise and other  
33 elements of climate change along this coast.

34 **Keywords:** earthflow, coastal-valley, UAV, LiDAR, SfM-Photogrammetry, Galicia.

35

## 1. Introduction

Steep slopes produced by marine undercutting are conducive to many types of mass movement in coastal regions. The type, size, and frequency of these movements, and subsequently the rate and mode of cliff evolution and sediment supply to the coast, reflect the absolute and relative efficacy of the subaerial and marine process suites. The importance of these mechanisms varies according to the climate, which drives marine and subaerial processes, and the structure and other characteristics of the rock, which determine their resistance to weathering and erosion (Vann Jones et al., 2015; Hampton and Griggs, 2004; Sunamura, 1992; Trenhaile, 1987; Emery and Kuhn, 1982).

Rockfalls triggered by marine undercutting are dominant on many exposed coasts, but translational and rotational landslides can predominate where geological conditions are suitable. Earthflows are intermittent slope movements of plastic, clayey soils that can develop at the bulbous front of slumps or at the foot of steep, eroding cliffs. They are generally less common than falls and slides on rocky coasts, although they can develop from landslides or other loose debris where water flows are concentrated on the floor of short, steep valleys.

Flows in coastal areas vary according to their morphology, topography, rheology, and sedimentology (Germain and Ouellet, 2013). Material moves within earthflows as a result of the intermittent flow-like movement of plastic, clayey soil, internal shear strains, and sliding along single or multiple shear surfaces. This produces lobate structures with typical rates of movement ranging, from meters per hour during active periods to meters per year in general (Hung et al., 2014; Keefer and Johnson, 1983; Varnes, 1978).

Whereas many mass movements are rapid and can only be examined after they have occurred, they can be measured and monitored in slow earth flows as they take place. There have been notable advances in recent years in our ability to retroactively identify and measure slow changes in topographic elements. They include developments in geomatics (e.g. TPS, GPS-RTK, TLS), remote sensing (high resolution satellite images, Airborne-LiDAR), and photogrammetry (automated digital photogrammetry, unmanned aerial vehicle –UAV–). The newest techniques, often involving Structure from Motion-Multi View StereoScan (SfM-MVS onwards) and UAVs, produce low cost and high quality-quantity topographical information. This

technology plays a key role in assessing, monitoring, and analysing global change and, accordingly, there has been an exponential increase in their use in the geomorphological disciplines, including mass movements (Turner et al., 2015; Abellán et al., 2014; Lucieer et al., 2014; Daehne and Corsini, 2013; Niethammer et al., 2012; Prokop and Panholzer, 2009; Baldi et al., 2008) and coasts (Castelle et al., 2017; Sturdivant et al., 2017; Autret et al., 2016; Casella et al., 2016; Ierodiaconou et al., 2016; Turner et al., 2016; Gonçalves and Henriques, 2015; Pérez-Alberti et al., 2015a,b; Harwin and Lucieer, 2012; Delacourt et al., 2009).

The purpose of this paper is to discuss the earthflow-like movement of debris on the northwestern coast of Spain. More specifically, it is concerned with spatial and temporal changes to slope behavior, including to rates of movement at annual to decadal scales, and the interaction between terrestrial mass movement and marine erosional processes. Historical air photographs, LiDAR, and images obtained with an UAV and SfM-MVS techniques were used to identify temporal and spatial changes in rates of movement in the distal fan or lobate debris cone over a 61-year period. This was supplemented by precipitation and wave data to relate these changes to a variety of environmental conditions. The research was conducted in a rocky coastal-valley environment, and therefore differs from previous attempts to record temporal and spatial patterns of movement in slow mass movements (Handwerger et al., 2015; Prokešová et al., 2014; Mackay and Roering, 2011; Coe et al., 2009) in that wave erosion and the removal of lateral support from the toe of the flow must be considered in addition to variations in rainfall intensity and frequency. Additionally, although this earthflow is a locally significant source of sediment on a slowly eroding coast, its size is constrained by the high coastal cliffs in the study area and by the correspondingly short length and small catchment area of the valley that is incised into them. This earthflow is therefore much smaller than the long earthflows frequently described in more terrestrial environments (Keefer and Johnson, 1983; Handwerger et al., 2015). The terms *deposit*, *debris lobe* and *flow* are used in places to refer to the earthflow in this paper, with the latter term used to refer to its movement, irrespective of whether it is accomplished primarily by sliding or flowing.

## **2. Study site**

The study was made in northwestern Galicia, Spain, in a region considered to be of such geological, pedological, archeological, and biological interest that it has been proposed as a future Geopark, a legal designation under the auspices of UNESCO (Horacio et al., 2019). The climate of this region is humid oceanic, with abundant precipitation (~2,000 mm per year) and mild temperatures (~14 °C), punctuated with microclimates related to slope aspect and proximity to the ocean.

The study was concerned with the lower portion of an unnamed valley (henceforth referred to as the Teixidelo valley) terminating at the rear of an adjacent boulder beach, about 1.8 km east of the village of Santo André de Teixido (Fig. 1A). The valley has been incised into a cliff cut into a gently sloping plateau (with cliff-top gradients < 8° to 16°). The cliffs in this region have a maximum elevation of 612 m (Vixía Herbeira), and are among the highest on the European mainland. The cliff face is generally steep, with gradients ranging up to the sub-vertical in places. The valley is oriented perpendicularly to the shore and is about 1 km in length. It is steep and narrow in the header zone but more gently sloping (20 to 30°) and wider nearer the coast. The valley runs along a NW-SE oriented fault with a 65° dip, which was formed during an extensional phase in the Variscan orogeny. The rocky substratum in the valley consists of ultramafic, granulitic and phyllonitic quartz rocks (Fig. 1B).

The floor of the valley is occupied by a bulbous, hummocky deposit, about 200 m in length (Fig. 1A and Fig. 2A). Active and inactive sections of the deposit were identified according to the occurrence of slope fissures and related scarps (Fig. 1), and by distinguishing between elements (e.g. large boulders) that are moving from those that are not, based on remote sensing data. Air photographs show that several boulders further up the valley have been stationary since at least 1956, and that this essentially inactive section does not contribute to movement in the debris lobe further seawards. Two subareas can be distinguished in the active zone. The upper one, extending seawards from the head of the active zone, has many cracks, gullies, and other breaks in the soil cover of various shapes and dimensions, and a scarp composed of clay which forms the base of the moving mass (Fig. 2B). The second area, further seawards, is an accumulation zone containing numerous boulders of different sizes, and diverse lobes, indicative of multiple shear surfaces, moving toward the sea, where it is exposed to, and periodically truncated by, storm waves (Fig. 2C and 2D).

Data from field measurements and LiDAR based DEMs (Digital Elevation Models) suggest that the deposit is variable in thickness, being about 13 m in the central part of the flow and as much as 20 m in the southern sector. There are linear ridges running along its sides, parallel to the valley, and curved, transverse ridges in the lower, central part. Most of its surface is covered by grass and small bushes, with some willows (*Salix sp.*) and hazels (*Corylus avellana*) at the head of the valley. The deposit contains angular and subangular rock fragments ranging up to large boulders with their major axes > 3 m (Fig. 2E). These clasts are in a greenish-gray montmorillonite clay matrix that is rich in magnesium phyllosilicates and very plastic when saturated. The rock fragments in the deposit are representative of the local valley substrata, including granular amphibolites and intensely fractured pyroxenite-peridotites, with a predominance of amphibolites on the southern side of the valley and pyroxenite-peridotites on the northern side.

### 3. Methods

The basic data used to monitor movements in the valley-floor deposit were obtained from aerial surveys (Table 1). Orthophotographs were available for 1956, 2008, 2010, 2014, and 2017 and for LiDAR in 2010. Other air photographs from 1945, 1983, 1984, 2002, and 1990, were rectified for this study. All images from the period 1945-2014 and 2017 were obtained from the relevant state organism (The National Geographic Institute and, for 1945, the Cartographic and Photographic Center). Additional high resolution data were obtained in 2016 and 2018 using a low flying UAV (Tables 1 and 2). Because of their resolution and low quality, it was concluded that the 1945, 1984, and 2002 images should not be used in this paper, and that 1956 would therefore represent year zero for this study.

Two procedures were used to quantify movement in the valley deposits. The first was concerned with locating and recording the position in a GIS environment of the centroid of selected features on the valley floor, on a two-dimensional xy plane. A variable scale (a maximum from 1/60 in 2016 and a minimum of 1/500 in 1956) was used to map the location of these features on each image in order to identify and compare changes in their location through time. The same line and polygon were used for all the images; both shapes (line and polygon)

were drawn using the highest quality image (2016). The features that were selected were clearly recognizable and re-locatable on the studied images, including large boulders (clasts, referenced as C1 to C4) and topographic lobes (referenced as L1 to L3) with well-defined ridges (Fig. 4). The only anthropogenic feature was the stone wall base of a small, ruined building (henceforth referred to as a hut), which was constructed for a former nickel mining operation. Peak activity was in the mid-nineteenth century and mining ceased at the end of the 19<sup>th</sup> century. The location of the coast was represented on the images by a well-defined, erosional scarp which forms the front of the debris lobe (Fig. 2E). Mean rates of movement over specified time periods are given to two decimal points. This does not represent the degree of measurement precision, which varies with the particular aerial survey, but is rather the product of dividing the amount of movement over a period by the corresponding time interval.

The second procedure was based on the DEM of Difference (DoD) produced from DEMs from the 2010 LiDAR flight and the 2016 and 2018 UAV flights. Georeferencing of the UAV data was based on 38 (2016 flight) and 19 (2018 flight) ground control points measured using Global Positioning System - Real Time Kinematics (GPS-RTK) and a Total Station (total RMSE - the root mean square error - 3 cm) (Table 2). Density and spatial distribution of the ground control points followed previous studies to try to obtain the lowest RMSE (Vericat et al., 2009). The data were processed using Agisoft PhotoScan Pro 1.2.6 software. An orthoimage with 10 cm spatial resolution was generated as a by-product of the SfM-MVS technique (Gonçalves and Henriques 2015; Turner et al. 2015). This second procedure provided a more precise estimate of the rate of movement than the first procedure, although it was representative of only a much shorter time frame (8 yrs). ArcGIS 10.5 software and a version of the Toolbox Geomorphic Change Detection (GCD) developed by Wheaton et al. (2010), was used on the DoDs to identify and map changes in the total and relative elevation, area, and volume of the earthflow, and consequently to calculate the net sedimentary balance in the study area. LoDMin of  $\pm 25$  cm was used for the Minimum Level of Detection (LoDMin), the smallest change in elevation that can be detected in the topographic models, based on the RMSE of the check points of the DEMs.

There were no continuous precipitation records from the study area, so one was compiled by combining data from four stations in adjacent areas (Table 3). Daily rainfall and the cumulative



deviation from the mean of daily rainfall were used to provide a measure of variation over the study period (Massey et al., 2013). Deep-seated earthflows often require prolonged periods of precipitation, however, in order to raise pore-water pressures sufficiently to trigger movement along the basal shear zone (Handwerger et al., 2015). Therefore, to consider the effect of persistent and heavy rainfall events, five-day and ten-day running totals were calculated for the entire study period.

Wave data were obtained from the National Oceanographic Institute (Puertos del Estado). Although there is a buoy at Estaca de Bares, about 44 km from the study area, it has only been operating since 1996 and there are significant gaps in the record. Consequently, simulated data were used in this study from SIMAR point 3036042, only about 4 km from the study area. These data represent a temporal (hourly) series of wind, surf, and sea level parameters derived from numerical models rather than from direct measurement of wave conditions (Gómez-Lahoz and Carretero-Albiach, 2005). Because the SIMAR data only extend back to 1958, data were lacking for the period of study from 1956-10-13 to 1957-12-31. The SIMAR data used in this study were spectral significant wave height and mean direction. The National Oceanographic Institute considers that SIMAR data provide adequate descriptions of actual wave conditions for almost all parts of Spain. This was confirmed for northern Galicia through an analysis conducted in the present study, which found that there was a high correlation (non-parametric Spearman's rank correlation coefficient 0.92) between modeled (SIMAR 3036042) and recorded mean daily significant wave height at the Estaca de Bares buoy. Nevertheless, there was a tendency, possibly related to differences in the physical characteristics of the buoy and the simulation site, for the model to underestimate the height of the highest waves (Fig. 3). Variations in wave conditions were represented in the present study by changes in the maximum daily wave height over the study period, and in the daily frequency of waves of more than 8 m in height.

Coastal erosion periodically trims back the base of the earthflow, removing lateral support (debuttressing) and possibly promoting more rapid movement of the wet, plastic debris (Fig. 2E and 2F). To assess the effect of this factor, changes in the location of the erosional bluff or, following a period of deposition, the leading edge of the flow, were recorded over each of the survey periods at ten locations (lines) spaced approximately 24 m apart along the coast. These

data were then compared with the rates and direction of movement of the deposit recorded over the same periods.

#### 4. Results

Based on the DEM of the 2010 LiDAR survey and the tool Surface Volume (ArcMap 10.5), the volume of the mobile deposit on the floor of the Teixidelo valley is about  $11 \times 10^6 \text{ m}^3$ , compared with the  $48 \times 10^6 \text{ m}^3$  volume of the valley and the  $172 \times 10^6 \text{ m}^3$  of the much larger scar which encloses the valley and a large deposit on its eastern side (Fig. 1A). These estimates suggest that, assuming the deep valley was the source of the material in the earthflow, about 94 % of the material eroded and transported from the valley, by mass movements or by fluvial or even glacial mechanisms (Pérez-Alberti, 2014), has been removed already by the sea. Conversely, if the mobile deposit was derived entirely from the Teixidelo valley, then about 77 % of the material would have been removed.

The mean rate of movement since 1956 for the eight recorded points, was  $0.48 \text{ m yr}^{-1}$ , which has resulted in a displacement of about 30 m down the valley (Table 4, Fig. 4A). Mean rates increased from only  $0.14 \text{ m}\cdot\text{yr}^{-1}$  from 1956 to 1983, to between  $0.50$  and  $0.87 \text{ m}\cdot\text{yr}^{-1}$  from 1983 to 2018. The mean rates, and consequently the corresponding distances of travel, have been broadly similar for each of the eight monitored points over the study period, ranging between only  $0.43$  and  $0.50 \text{ m}\cdot\text{yr}^{-1}$  (Table 4). There was no consistent trend in the rates of movement in this area from the rear to the front of the deposit. For example, although the most landward points, C1 and L1, had slightly higher overall rates of movement than the most seawards, L2 and L3, from 1956 to 2018, the landward and seaward rates varied, relative to each other, from 1956 to 1983 and 1983 to 2018.

Although there were some temporal and spatial changes, the general direction of movement was north-northwesterly over the monitoring period. The most significant changes, involving a slight shift of the centroids to the west before the flow reverted to its former direction, were by C1, C2, and C3 between 1983 and 1990, and a change to a more westerly direction by several tracked points, but especially by L2 and L3, between 2016 and 2018 (Table 5, Fig. 4B).

Based on the DoDs from the 2010 LiDAR and the 2016 and 2018 UAV surveys, most of the debris lobe experienced positive or negative changes in elevation, ranging up to almost 5 m from 2010 to 2016 and almost 4 m from 2016 to 2018 (Fig. 5 and Fig. 6). The changes were broadly similar over the two periods, with surface elevation dominating in the depletion zone in the southern interior. Areas of surface lowering and elevation coexisted in the outer, accumulation zone, across the toe of the deposit (Table 6, Fig. 5 and Fig. 6). These areas were distributed in an irregular but broadly crescentic pattern parallel to the front, forming an undulating surface, although the prominent band which experienced a loss in elevation was more continuous and wider in 2010-2016 than in 2016-2018 (inset C provides a detailed view of a section of this band in Figs. 5 and 6). The crescentic pattern was punctuated by a few ridges running parallel to the direction of movement, along either side of the deposit. These ridges were increasingly elevated between 2010 and 2016 and in general from 2016 to 2018, although a few experienced some lowering during this latter period. Another distinctive area, around a very large boulder (C4) near the western edge of the deposit, experienced slight uplift from 2010 to 2016 but was characterized by an irregular, essential random patchwork of elevated and depressed areas from 2016 to 2018 (inset map A in Fig. 5 and Fig. 6).

The heaviest rainfall, based on the number of days each year in which there was more than 70 mm, occurred during several periods between 1991 to 2018, and particularly from 1983 to 1991 when the area experienced the remnants of Hurricanes Klaus and Hortensia in 1984, and an intense NW storm in February 1989 (Fig. 7A). Cumulative deviation from the daily mean rainfall was generally below the mean from 1957 to 1985 and above it, attaining a maximum around 2004, from 1986 to 2018 (Fig. 7A). The most frequent high rainfall events, totaled over 5-day and 10-day periods were between 1983 and 1990 and from 2014 to 2016 (Table 7).

Maximum daily, monthly, and annual wave heights were broadly similar over the entire study period (1958-2018), although the extreme values (frequency of waves > 8 m) were a little higher in the period before than after 1990, and especially between about 1984 and 1990 (Fig. 8). The coast experienced periods of erosion and deposition during the monitoring period, varying in space and time, with faster rates of wave erosion generally occurring over shorter periods than slower rates of earthflow-induced deposition. Consequently, there were only fairly minor long-term changes in the position of most of the shore along the front of the debris lobe, with the

exception of marked erosion in the east-central portion (lines 7 to 9), where the coast has retreated from almost 16 m to more than 22 m since 1956 (Fig. 9).

There was little evidence, based on a comparison of erosion rates during periods of coastal erosion and deposition, to suggest that debuttreasing has caused rates of movement to increase. The hut and lobes L2 and L3 are only about 20-25 m from the coast and might therefore be expected to respond to debuttreasing. The hut is almost directly behind coastal line 7, which has experienced almost continuous coastal erosion and retreat since the 1983-1990 period. Conversely, L2 is behind line 6 and L3 is between lines 4 and 5, which have experienced offsetting periods of coastal advance and retreat over the study period (Fig. 4B and Fig. 9). The mean rate of movement of the hut was a little higher than for L3, despite the occurrence of more than 3 m of erosion on line 5 between 2005 and 2008 when, paradoxically, the rate of movement at L3 declined, and mean rates were identical for the hut and L2 (Table 4). Similarly, coastal erosion did not appear to be responsible for higher rates of movement than deposition over each monitoring interval. For example, L2 and L3 experienced high rates of movement ( $1.04\text{--}1.37\text{ m}\cdot\text{yr}^{-1}$ , respectively) during a period of coastal stability or only minor erosion in their adjacent coastal zones from 2017-2018, and low rates of movement ( $0.49\text{--}0.32\text{ m}\cdot\text{yr}^{-1}$ , respectively) during a period of erosion in these coastal zones from 2005-2008. The general lack of a direct relationship between rates of earthflow movement and coastal erosion is also consistent with the lack of a response by hut movement to about 2.5 m of coastal erosion along line 8 from 2017-2018 (Fig. 9).

Despite the lack of a clear relationship between rates of movement and coastal erosion, other evidence suggests that debuttreasing may have an effect on earthflow dynamics. Rates of earthflow movement generally decrease towards the toe (Keefer and Johnson, 1983). The tendency for rates to be fairly uniform from the rear to the front of the Teixidelo earthflow (Table 4) is therefore atypical, and may imply that truncation and undermining of the deposit by coastal erosion help to draw it downslope, thereby facilitating movement in the seaward extremity at rates that are higher than would otherwise occur. Debuttreasing may also have influenced the direction of earthflow movement, as plastic debris was diverted away from coastal areas that were stable or advancing seawards towards adjacent areas that were eroding. There is some evidence to support this contention in the study area. For example, the more than 3 m of

erosion that occurred between 2005 and 2008 along coastal line 5 may explain why L3 swung towards (41°) the northeast. Conversely, while L2 swung away from line 5, it moved north-northeasterly (19°) towards line 7, which had been experiencing almost continuous, albeit minor, erosion since 1983 to 1990 (Table 5, Fig. 4B and Fig. 9). Nevertheless, other changes cannot be attributed to coastal erosion. They include those by C1, C2, and C3 in the southern and eastern interior of the flow between 1983 and 2005, which were probably generated by internal pressures, and other directional changes over short distances that likely resulted from rotation of the tracked points on the flow and resulting changes in the location of the associated centroids.

## **5. Discussion**

This study has been concerned with decadal-scale monitoring of patterns and rates of movement in a coastal earthflow, using historical air photographs and high resolution LiDAR and UAV-based airborne systems. While remote sensing is a valuable tool to monitor long-term changes in coastal systems, including earthflows and other slow mass movements, the temporal resolution is too coarse to provide definitive evidence of the responsible mechanisms, which operate over much shorter timescales. Valuable inferences can be drawn, however, from the morphology of the deposit, temporal and spatial variations in flow dynamics, and meteorological and oceanographic data on rainfall and wave heights. Remotely sensed data in coastal regions can therefore be used to identify and focus on areas of particular interest for more detailed field study, to estimate rates of coastal retreat and the contribution of mass movements to coastal sediment budgets, and to assess the possible risks posed to coastal communities and infrastructure by rising sea level and increased storminess.

The mobile deposit in the Teixidelo valley can be described, according to the classification of Hungr et al. (2014), as a slow earthflow. This conclusion is consistent with its morphology, the different directions and overall rates of movement, and the presence of a clay matrix which is very plastic when saturated. The flow-parallel ridges running along the sides of the deposit are fairly common features on earthflows (Keefer and Johnson, 1983). As they are generally still rising in this area, (Fig. 5 and Fig. 6) and are covered in vegetation, they are probably the

product of internal pressures generated within the flow, rather than of material overflowing onto the adjacent ground surface. It is generally accepted that earthflows, as well as other types of mass movement, are triggered and are therefore most prevalent during periods of high rainfall. The relationship in the study area between rates of movement and increases in the occurrence of heavier rainfall in the 1980s is therefore predictable and consistent with the literature (Table 7, Fig. 7B) (Bayer et al., 2018; Hürlimann et al., 2016; Handwerger et al., 2015; Giordan et al., 2013; Massey et al., 2013; Keefer and Johnson 1983). Nevertheless, because only 9 time intervals were available for this study, Spearman's rank correlations ( $\rho$ ) were insignificant for rates of earthflow movement against: time ( $\rho$  0.23;  $P$  0.55); rainfall (number of cumulative 5-day rainfall events > 70 mm) ( $\rho$  0.13;  $P$  0.75); and storm frequency (number of large storms with waves > 8 m) ( $\rho$  0.11;  $P$  0.78). An anthropogenic event may also have triggered an increase in debris mobility in this area, although it cannot account for the continuation of similar rates of movement more than 3 decades later. This occurred in January 1986, when the 185 m-long freighter Bonnie Carrier ran aground directly in front of the Teixidelo valley. The wreck created a barrier against wave attack and its subsequent removal required construction of an extensive track system in the valley which destabilized the deposit in places (Fig. 10).

In a coastal environment, one might also expect rates of earthflow movement to increase following periods of wave-induced erosion and destabilization of the slope deposits. There is no direct evidence that wave erosion is responsible for increased rates of movement of the Teixidelo earthflow, although this effect may have been obfuscated by the fairly low temporal resolution of the remotely sensed data. Given that rates of movement generally decrease down earthflows (Keefer and Johnson, 1983), the occurrence of quasi-uniform rates may be indicative of the lack of a lower, slower moving section due to the proximity of the coast, or it could be the result of debuttreassing by wave erosion. Erosional truncation of the earthflow and the presence of a steep scarp at the coast suggest that both of these factors must be significant (Fig. 2D and 2E). While wave erosion probably promotes increased output from the terrestrial to the littoral system, however, the effect may be short-lived due to the greater protection from the waves afforded by the large, essentially immobile boulders dislodged from the flow, which accumulate at the cliff foot (Fig. 2F). According to this hypothesis, coastal earthflows containing significant amounts of coarse material may experience cyclical perturbations in activity that are

superimposed on those due to precipitation. The amplitude and frequency of these cycles will reflect the amount of protective material at the cliff foot and its rate of removal, which will depend, in turn, on such factors as the wave climate, the thickness of the earthflow toe, and the amount and size of the coarse material in it (Fig. 11).

The toe of the earthflow extends along the coast for about 215 m, and its mean height at the shore is 11.2 m (Fig. 2D and 2E). Based on measured rates of earthflow movement (Table 4) and estimates that coarse material constitutes roughly 20 % of the sediment (Fig. 2E), the flow will have contributed more than 14,000 m<sup>3</sup> of coarse sediment to the littoral budget since 1956 and almost 13,000 m<sup>3</sup> since 1983; this corresponds to an annual supply of 1.1 m<sup>3</sup> and 1.7 m<sup>3</sup> of debris per 1 m of coast, respectively. Fine material in the earthflow erodes fairly continuously but it is carried offshore in suspension, whereas the erosion of coarse material, which stays on the beach, is more episodic. Because these erosional events tend to be of high magnitude and low frequency, clast accumulation and removal is likely to produce temporally and spatially variable amounts of toe protection, and consequently rates and directions of earthflow movement.

Rock coasts are generally expected to experience more rapid rates of erosion with climate change. There are many possible complexities however which could trigger differences in coastal response in space and time. Rising sea level and possibly increased storminess will trigger attendant changes in wave refraction patterns, tidal range and sediment production, transport and accumulation, while changes in temperature and precipitation will affect coastal mass movements, weathering rates and bioprotectonal and bioerosional processes; these complex, interacting mechanisms could act to increase erosion rates in some areas and decrease them in others (Trenhaile, 2014). The results of the work described in this paper suggest that the composition of coastal earthflows will have important implications regarding their response to climate change and their ability to provide sediment to the littoral environment. Climate change may lead to increased precipitation in some places, and consequently greater earthflow activity, while higher sea level and increased storminess will promote wave erosion and changes in the water table and pore water pressures. These effects may be countered in some types of earthflow by the accumulation of coarse sediment on the beach, but the

protective effect is likely to be insignificant where the material is dominantly fine-grained and able to be transported offshore in suspension.

## 6. Conclusions

The main conclusions of this paper are:

- a. Mean rates of movement of the coastal earthflow in the Teixidelo valley increased from 0.14 m·yr<sup>-1</sup> between 1956 and 1983 to between 0.50 and 0.83 m·yr<sup>-1</sup> from 1983 to 2018.
- b. The increase in transport rates corresponded to, and was presumably largely a result of, an increase in precipitation.
- c. Despite the general lack of a relationship between transport rates and coastal erosion, other evidence suggests that debuttreasing may promote downslope sediment flux and trigger changes in direction.
- d. The movement of coastal earthflows containing large quantities of coarse material may be constrained by negative feedback, whereby erosionally induced debuttreasing and faster earthflow movement results in greater accumulation of coarse, protective debris on the beach and, subsequently, reduced rates of coastal erosion.

## Acknowledgements

The authors thank Ramón Blanco Chao 'Mochi', Dominic Royé, Alejandro Gómez Pazo, Víctor Bouzas Blanco, Sam McColl, Miguel San Claudio Santa Cruz and Pilar Gil (National Oceanographic Institute) for their suggestions and efficient solutions to our technical questions. To the entire team at the National Geographic Institute for public relations for their kindness and efficiency in the request of information and clarification of doubts. To Francisco Canosa 'Fran', geologist and main promoter of the proposal for a Geopark at the study site, for the relevant geological and historical information offered. He also provided the photo in Figure 2B. To José Manuel Freire Roca (Xestega Delineación S.L. Company) for providing,



topographic material without charge. To Bárbara Barrientos Low, María del Rosario Ibarra Ibarra and Marta Franch Sas for their diverse help. We especially thank José Manuel Sierra-Pernas 'Chema' for his support in the field and for office and logistics work, as well as his valuable comments to improve the article.

We also thank the anonymous reviewers for their comments and suggestions.

The first author is a beneficiary of the post-doctoral fellowship named *Programa de ayudas de apoyo a la etapa inicial de formación posdoctoral (2017)* founded by the *Consellería de Cultura, Educación e Ordenación Universitaria de la Xunta de Galicia* (Government of Galicia, Spain).

The second author is a beneficiary of the pre-doctoral fellowship FPU 13/00168 founded by the Ministry of Education, Culture and Sport of Spain.

## References

- Abellán, A., Oppikofer, T., Jaboyedoff, M., Rosser, J.N., Lim, M., Lato, J., 2014. Terrestrial laser scanning of rock slope instabilities. *Earth Surf. Process. Landf.* 39 (1), 80–97.
- Autret, R., Dodet, G., Fichaut, B., Suanez, S., David, L., Leckler, F., Filipot, J. F. (2016). A comprehensive hydro-geomorphic study of cliff-top storm deposits on Banneg Island during winter 2013–2014. *Marine Geology*, 382, 37–55. <https://doi.org/10.1016/j.margeo.2016.09.014>.
- Baldi, P., Cenni, N., Fabris, M., Zanutta, A., 2008. Kinematics of a landslide derived from archival photogrammetry and GPS data. *Geomorphology* 102, 435–444.
- Bayer, B., Simoni, A., Mulas, M., Corsini, A., Schmidt, D., 2018. Deformation responses of slow moving landslides to seasonal rainfall in the Northern Apennines, measured by InSAR. *Geomorphology* 308, 293–306.
- Casella, E., Rovere, A., Pedroncini, A., Stark, C. P., Casella, M., Ferrari, M., & Firpo, M. (2016). Drones as tools for monitoring beach topography changes in the Ligurian Sea (NW Mediterranean). *Geo-Marine Letters*, 36(2), 151–163. <https://doi.org/10.1007/s00367-016-0435-9>.
- Castelle, B., Bujan, S., Ferreira, S., Dodet, G., 2017. Foredune morphological changes and beach recovery from the extreme 2013/2014 winter at a high-energy sandy coast. *Mar. Geol.* 385, 41–55.
- Coe, J.A., McKenna, J.P., Godt, J.W., Baum, R.L., 2009. Basal-topographic control of stationary ponds on a continuously moving landslide. *Earth Surf. Process. Landf.* 34, 264–279.
- Concello de Cariño (2010). Patrimonio e desenvolvemento local: reflexións e iniciativas no Concello de Cariño. *Actas das I e II Xornadas de Patrimonio e Desenvolvemento Local*. Concello de Cariño, 154 p.
- Daehne, A., Corsini, A. 2013. Kinematics of active earthflows revealed by digital image correlation and DEM subtraction techniques applied to multi-temporal LiDAR data. *Earth Surf. Process. Landforms* 38, 640–654.
- Delacourt, C., Allemand, P., Jaud, M., Grandjean, P., Deschamps, A., Ammann, J., Cuq, V., Suanez, S., 2009. DRELIO: an unmanned helicopter for imaging coastal areas. *J. Coastal Res. Spec. Issue* 56, 1489–1493.

451 Emery, KO., Kuhn, GG. 1982. Sea cliffs: their processes, profiles, and classification. *Geol. Soc. Amer. Bull.*  
452 93, 644–54

453 Germain, D., Ouellet, M.-A. 2013. Subaerial sediment-water flows on hillslopes: Essential research  
454 questions and classification challenges. *Progress in Physical Geography: Earth and Environment* 37, 813–  
455 833.

456 Giordan, D., Allasia, P., Manconi, A., Baldo, M., Santangelo, M., Cardinali, M., Corazza, A., Albanese, V.,  
457 Lollino, G., Guzzetti, F. 2013. Morphological and kinematic evolution of a large earthflow: The Montaguto  
458 landslide, southern Italy. *Geomorphology* 187 (2013) 61–79.

459 Gómez-Lahoz, M., Carretero-Albiach, J.C. (2005). Wave forecasting at the Spanish coasts. *Journal of*  
460 *Atmospheric and Ocean Science*, 10(4): 389- 405. DOI: 10.1080/17417530601127522.

461 Gonçalves, J.A., Henriques, R., 2015. UAV photogrammetry for topographic monitoring of coastal areas.  
462 *ISPRS J. Photogramm. Remote Sens.* 104, 101–111.

463 Hampton, M.A., Griggs, GB. 2004. Formation, Evolution, and Stability of Coastal Cliffs – Status and trends.  
464 United States Geological Survey. Professional paper 1693.

465 Handwerger, AL., Roering, JJ., Schmidt, DA., Rempel, AW. 2015. Kinematics of earthflows in the Northern  
466 California Coast Ranges using satellite interferometry. *Geomorphology* 246, 321–333.

467 Harwin, S., Lucieer, A., 2012. Assessing the Accuracy of Georeferenced Point Clouds Produced via Multi-  
468 View Stereopsis from Unmanned Aerial Vehicle (UAV) Imagery. *Remote Sensing* 4, 573-1599. ; DOI:  
469 10.3390/rs4061573.

470 Horacio, J., Muñoz-Narciso, E., Sierra-Pernas, J.M., Canosa, F., Pérez-Alberti, A. 2019: Geo-Singularity of  
471 the Valley-Fault of Teixidelo and Candidacy to Geopark of Cape Ortegal (NW Iberian Peninsula):  
472 Preliminary Assessment of Challenges and Perspectives. *Geoheritage*, [https://doi.org/10.1007/s12371-](https://doi.org/10.1007/s12371-019-00349-2)  
473 019-00349-2.

474 Hungr, O., S. Leroueil, and L. Picarelli. 2014. The Varnes classification of landslide types, an update.  
475 *Landslides* 11:167–194.

476 Hurlimann, M., Lantada, N., Gonzalez, M., Pinyol, J. 2016. Susceptibility assessment of rainfall-triggered  
477 flows and slides in the Central-Eastern Pyrenees. A: *International Symposium on Landslides. Landslides*  
478 *and Engineered Slopes. Experience, Theory and Practice: Proceedings of the 12th International*  
479 *Symposium on Landslides (Napoli, Italy, 12-19 June 2016). Napoli: CRC Press, Aversa, S. (ed.), p. 1129-*  
480 1136.

481 Ierodiaconou, D., Schimel, A. C. G., & Kennedy, D. M. (2016). A new perspective of storm bite on sandy  
482 beaches using Unmanned Aerial Vehicles. *Zeitschrift Für Geomorphologie, Supplementary Issues*, 60(3),  
483 123–137. [https://doi.org/10.1127/zfg\\_suppl/2016/00247](https://doi.org/10.1127/zfg_suppl/2016/00247)

484 Keefer, DK., Johnson, AM. 1983. Earth Flows: Morphology, Mobilization, and Movement. US. Geological  
485 Survey Professional Paper 1264 United States Government Printing Office, Washington.

486 Llena, M., Vericat, D., Martínez-Casasnovas, J.A. (2018) Aplicación de algoritmos Structure from Motion  
487 (SfM) para el análisis histórico de cambios en la geomorfología fluvial. *Cuaternario y Geomorfología*, 32  
488 (1- 2): 53-73.

489 Lucieer, A., De Jong, S.M., Turner, D., 2014. Mapping landslide displacements using structure from Motion  
490 (SfM) and image correlation of multi-temporal UAV photography. *Prog. Phys. Geogr.* 38 (1):97–116.  
491 <http://dx.doi.org/10.1177/0309133313515293>.

492 Mackay, B.H., Roering, J.J., 2011. Sediment yield, spatial characteristics, and the long-term evolution of  
493 active earthflows determined from airborne LiDAR and historical aerial photographs, Eel River, California.  
494 *Geol. Soc. Amer. Bull.* 123, 1560-1576.

495 Massey, Cl., Petley, DN., McSaveney, MJ., 2013. Patterns of movement in reactivated landslides.  
496 Engineering Geology 159, 1–19.

497 Niethammer, U., James, M.R., Rothmund, S., Travelletti, J., Joswig, M., 2012. UAV-based remote sensing  
498 of the Super-Sauze landslide: evaluation and results. Eng. Geol. 128, 2–11.

499 Pérez-Alberti, A., 2014. Geomorfología, in: Ferreiro, D.A., Macías, F., Calvo de Anta, R., Pérez-Alberti,  
500 A., Otero-Pérez, X.L., Verde-Vilanova, J.R., Pérez-Llaguno, C., Saiz-Rubio, R., Díez, E., Bolaños-Guerrón,  
501 D., (Eds.), Complejo Básico-Ultrabásico de Capelada-Cabo Ortegal. Andavira Editorial, Santiago de  
502 Compostela, pp. 24-30.

503 Pérez-Alberti, A., Trenhaile, A. S. (2015a). Clast mobility within boulder beaches over two winters in  
504 Galicia, northwestern Spain. Geomorphology, 248, 411–426.  
505 <https://doi.org/10.1016/j.geomorph.2015.08.001>

506 Pérez-Alberti, A., Trenhaile, A. S. (2015b). An initial evaluation of drone-based monitoring of boulder  
507 beaches in Galicia, north-western Spain. Earth Surface Processes and Landforms, 40(1), 105–111.  
508 <https://doi.org/10.1002/esp.3654>

509 Prokešová, R., Kardoš, M., Tábor, P., Medvedová, A., Stacked, V., Chudy, F., 2014. Kinematic behaviour  
510 of a large earthflow defined by surface displacement monitoring, DEM differencing, and ERT imaging.  
511 Geomorphology 224, 86–101.

512 Prokop, A., Panholzer., 2009. Assessing the capability of terrestrial laser scanning for monitoring slow  
513 moving landslides. Nat. Hazards Earth Syst. Sci., 9, 1921–1928.

514 San Claudio Santa Cruz, M. (1997). Tesouros asolagados. Historia dos naufraxios no mar de Galicia. Ed.  
515 Lea, Santiago de Compostela.

516 Sturdivant, E. J., Lentz, E. E., Thieler, E. R., Farris, A. S., Weber, K. M., Remsen, D. P., Henderson, R. E.  
517 (2017). UAS-SfM for coastal research: Geomorphic feature extraction and land cover classification from  
518 high- resolution elevation and optical imagery. Remote Sensing, 9(10). <https://doi.org/10.3390/rs9101020>

519 Sunamura, T., 1992. Geomorphology of rocky coasts. Wiley, New York.

520 Trenhaile, A.S., 1987. The Geomorphology of Rock Coasts. Clarendon Press, Oxford.

521 Trenhaile, A.S., 2014. Climate change and its impact on rock coasts, in: Kennedy, D. M., Stephenson, W.  
522 J., Naylor, L. (Eds), Rock Coast Geomorphology: A Global Synthesis. Geological Society, London,  
523 Memoirs, 40, pp. 7–17.

524 Turner, D., Lucieer, A., de Jong, S.M., 2015. Time series analysis of landslide dynamics using an  
525 unmanned aerial vehicle (UAV). Remote Sensing 7, 1736–1757.

526 Turner, I.L., Harley, M.D., Drummond, CD. 2016. UAVs for coastal surveying. Coastal Engineering 114,  
527 19–24.

528 Vann Jones (née Norman), E. C., Rosser, N. J., Brain, M. J., D. N. 2015. Quantifying the environmental  
529 controls on erosion of a hard rock cliff. Marine Geology 363, 230-242.

530 Varnes, D.J. 1978. Slope movement types and processes. In Landslides: Analysis and Control, 11–33.  
531 Washington, DC: Transport Research Board, National Academy of Sciences. Special Report.

532 Vericat, D., Brasington, J., Wheaton, J., Cowie, M. (2009). Accuracy assessment of aerial photographs  
533 acquired using lighter-than-air blimps: low-cost tools for mapping river corridors. River Research and  
534 Applications, 25(8): 985-1000

535 Wheaton, J.M.; Brasington, J.; Darby S.E.; Sear, D.A. (2010). Accounting for uncertainty in DEMs from  
536 repeat topographic surveys: improved sediment budgets. Earth Surface Processes and Landforms, 35,  
537 136-156. <https://doi.org/10.1002/esp.1886>.

Table 1. Available data sources and technical information. Where, georeference 1 was done specifically for this study and 0 by the relevant authority. The symbol - refers to unknown data, no data or not applicable (i.e. not valid for this field). Italics are used for unused flights with low image quality. RMSE is the root-mean-square error. UAV scale (S) was calculated through equation:  $S = \text{mean altitude flight} / \text{focal distance of the camera}$ .

Date	Flight name	Scale (cm)	Resolution**	Georef.	Method	GCPs	RMSE
1945-10-08	<i>Americano A</i>	<i>~1/43,000</i>	-	1	<i>Adjust ©ESRI</i>	26	<i>4.1195</i>
1956-10-13	Americano B	1/32,000	0.50-1.00	0	-	-	-
1983-11-15	Interministerial	1/18,000	0.25-0.50	1	Spline	41	0.0032
1984-09-12	<i>Nacional</i>	<i>1/30,000</i>	<i>0.50-1.00</i>	1	<i>Spline</i>	26	<i>0.3942</i>
1990-09-15	Costas	1/5,000	0.12	1	Spline	45	0.0134
2002-10-28	<i>Quinquenal</i>	<i>1/40,000</i>	<i>0.56-1.00</i>	1	<i>Spline</i>	23	<i>0.1115</i>
2005-05-24	PNOA	1/30,000	0.45	0	GNSS	-	≤ 1m
2008-07-22	PNOA	1/20,000	0.25	0	GNSS	-	≤ 1m
2010-08-10	PNOA*	1/20,000	0.25	0	GNSS	-	≤ 1m
2014-09-25	PNOA	1/20,000	0.22	0	GNSS	-	≤ 1m
2016-08-20	UAV	1/100	0.01	1	©APS***	38	0.0689
2017-06-18	PNOA	1/20,000	0.22	0	GNSS	-	≤ 1m
2018-03-03	UAV	1/90	0.01	1	©APS***	19	0.0571

\* Orthoimage + LiDAR data.

\*\* Pixel size (GSD) (m).

\*\*\* ©Agisoft PhotoScan (georeferencing is based by a model linear obtained from 7 parameters of transformation: 3 translation parameters; 3 of rotation and 1 of scale, Llana et al., 2018).

Table 2. UAV field and image data for 2016 and 2018.

Parameters	2016	2018
Flying height	39.2 m	35.3
No. images	183	278
Drone model	Phantom 3 advanced	Phantom 3 advanced
Camera	Casio FC300S	Casio FC300S
Camera resolution	4000 x 3000	4000 x 3000
Horizontal error	3.16 cm	4.10 cm
Vertical error	3.70 cm	3.00 cm

Table 3. Weather stations used in this study.

ID	Station	Location		Distance study area (km)	Missing data (days)	Date	
		Lat (N)	Lon (E)			From	To
1363 <sup>a</sup>	Pontes*	43.4462	7.8599	31.63	59	1956-10-13	1975-08-31
1353E <sup>a</sup>	Cedeira	43.6572	8.0466	9.47	0	1975-09-01	1984-10-31
1353 <sup>a</sup>	Capelada**	43.6734	7.9856	5.39	31	1984-11-01	2005-12-31
10097 <sup>m</sup>	Faladoira	43.5918	7.7887	20.26	0	2006-01-01	2018-03-03

\* Feb, Dec 1957 data are missing. Substituted with Capelada Station data.

\*\* Aug 2005 data are missing. Substituted with Pontes Station data.

<sup>a</sup> State Meteorological Agency (AEMET).

<sup>m</sup> Regional Meteorological Agency for Galicia (MeteoGalicia).

Table 4. Mean rates of movement ( $\text{m}\cdot\text{yr}^{-1}$ ) of the 8 points on the flow.

Year	Hut	C1	C2	C3	C4	L1	L2	L3	Mean
1956–1983	0.12	0.22	0.21	0.10	0.07	0.23	0.11	0.06	0.14
1983–1990	0.67	0.49	0.53	0.68	0.89	0.58	0.76	0.71	0.67
1990–2005	0.88	0.90	0.86	0.93	0.86	0.80	0.91	0.82	0.87
2005–2008	0.65	0.49	0.5	0.57	0.37	0.59	0.49	0.32	0.50
2008–2010	0.47	0.39	0.57	0.55	0.47	0.32	0.61	0.74	0.52
2010–2014	0.85	0.74	0.78	0.76	0.76	0.71	0.62	0.48	0.71
2014–2016	0.81	0.84	0.89	0.91	0.82	0.96	0.42	0.57	0.77
2016–2017	0.76	0.77	0.91	0.77	1.01	0.46	0.93	1.03	0.83
2017–2018	0.00	0.50	0.50	0.29	0.28	0.29	1.04	1.37	0.53
Mean	0.48	0.50	0.50	0.48	0.47	0.49	0.48	0.43	

562 Table 5. Azimuthal directions of movement for the 8 points on the flow.

Year	Hut	C1	C2	C3	C4	L1	L2	L3
1956–1983	333	338	0	339	336	315	330	298
1983–1990	324	271	318	320	328	323	326	335
1990–2005	338	339	329	339	321	327	335	324
2005–2008	354	358	356	8	16	314	19	41
2008–2010	6	330	306	313	276	318	336	244
2010–2014	332	335	337	343	335	342	291	337
2014–2016	336	348	347	346	350	303	323	308
2016–2017	266	265	269	272	233	326	221	236
2017–2018	-	219	208	153	328	278	273	268

563

564

565 Table 6. Sedimentary balance. For the DoDs, the resolution was 0.5 m<sup>2</sup> and the LoD<sub>Min</sub> was ± 25 cm.

Sedimentary balance	2010-2016	2016-2018
Total volume of surface lowering	5279	2441
Total volume of surface raising	2042	955
Total volume of LOD <sub>Min</sub> at ± 25cm	602	1035
Total volume difference	7321	3397
Total net volume difference	-3237	-1486

566

567

568

569

570

571

572

573

574

575 Table 7. Number of consecutive 5- and 10-day events with rainfall totals greater than 150 to 350 mm.

Year	Cumulative 5-day total			Cumulative 10-day total		
	Pr > 150	Pr > 200	Pr > 250	Pr > 250	Pr > 300	Pr > 350
	mm	mm	mm	mm	mm	mm
1956–1983	4.9	0.9	0.1	2.4	0.6	0
1983–1990	8.3	2.5	1.3	5.8	1.9	0.4
1990–2005	6.6	0.9	0.1	2.5	0.7	0.3
2005–2008	2.5	0.0	0.0	0.6	0.0	0.0
2008–2010	5.4	2	0.0	0.0	0.0	0.0
2010–2014	2.2	0.0	0.0	0.0	0.0	0.0
2014–2016	8.4	5.3	2.1	10.5	8.4	2.1
2016–2017	0.0	0.0	0.0	0.0	0.0	0.0
2017–2018	11.3	0.0	0.0	0.0	0.0	0.0

576

577

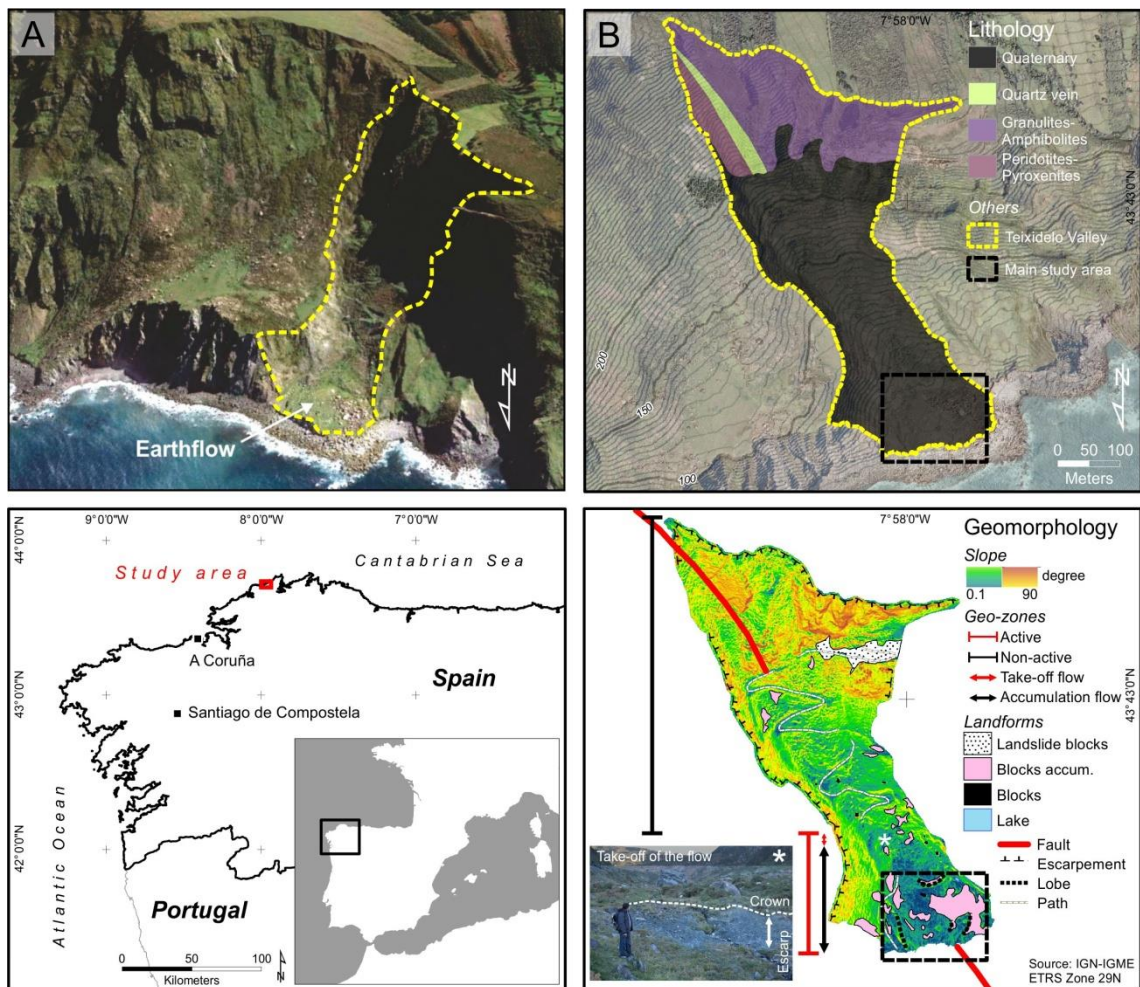


Figure 1. Oblique image (A) (source Google Earth), geological map (B), general location of the study area in northwestern Spain, and its slope and geomorphological characteristics. To avoid relief inversion, (A) and (B) are oriented so that north is at the bottom of the page.



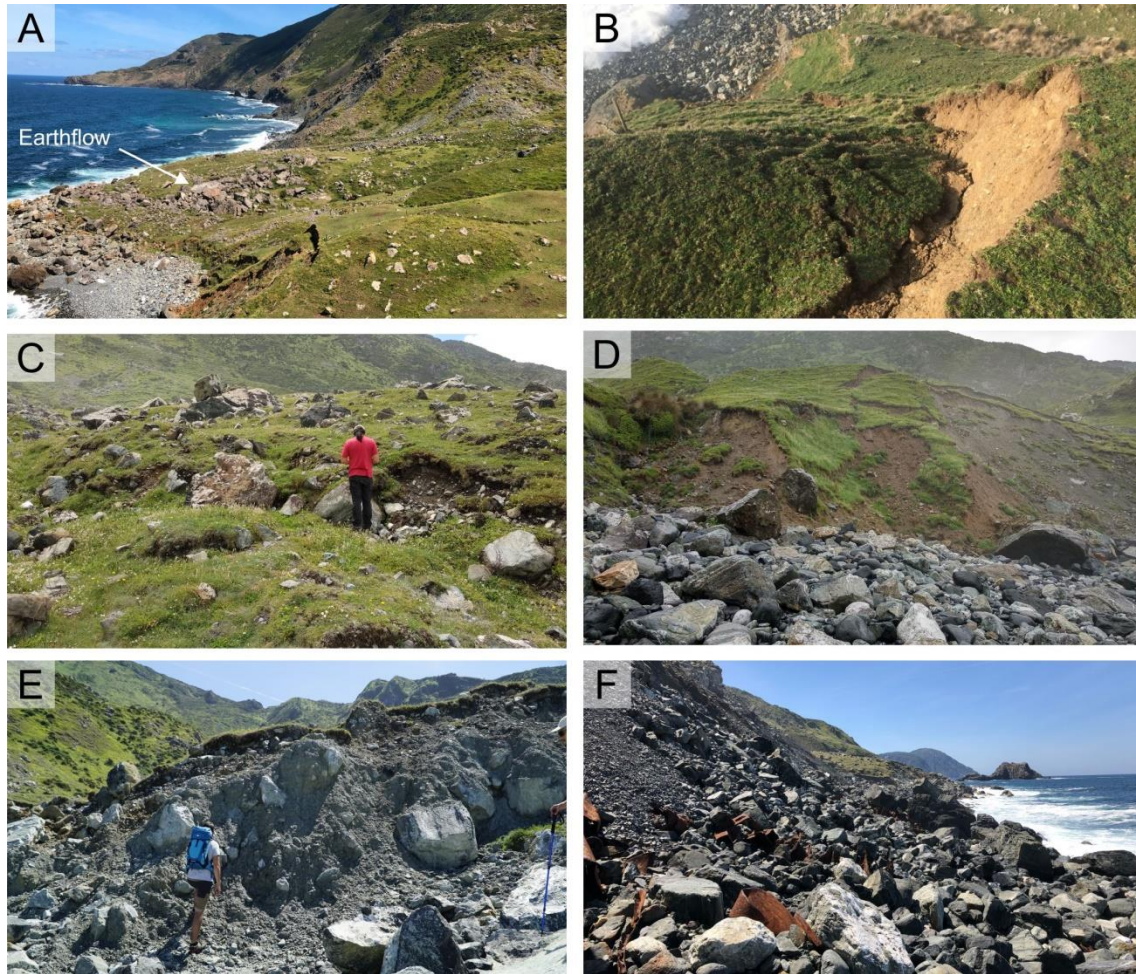


Figure 2. (A) The earthflow lobe extending to the coast; (B) the arcuate clay scarp at the rear of the zone of depletion; (C) hummocky lobes with exposed boulders in the accumulation zone; (D) the eroded, seaward toe of the flow and the adjacent boulder beach; (E) the eroded toe forming a cliff composed of large clasts in a clay matrix; (F) The coarse boulder beach at the cliff foot.

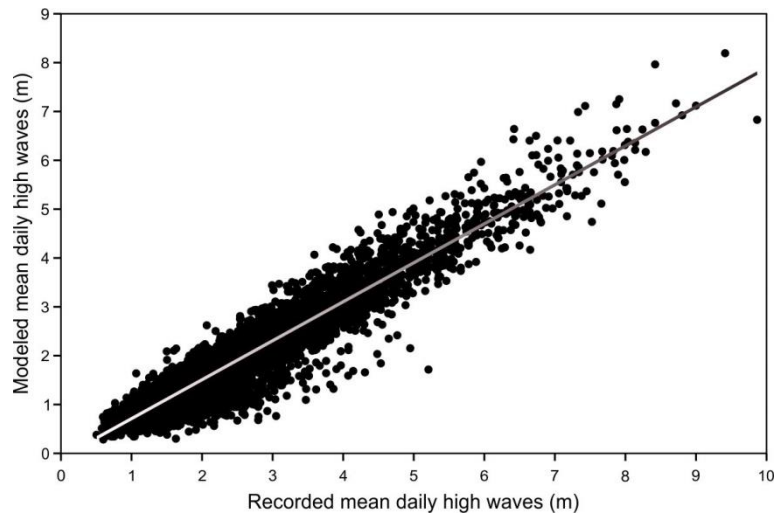


Figure 3. Mean daily significant wave heights with regression line modeled for SIMAR point 3036042 and recorded at the Estaca de Bares buoy since 1996.

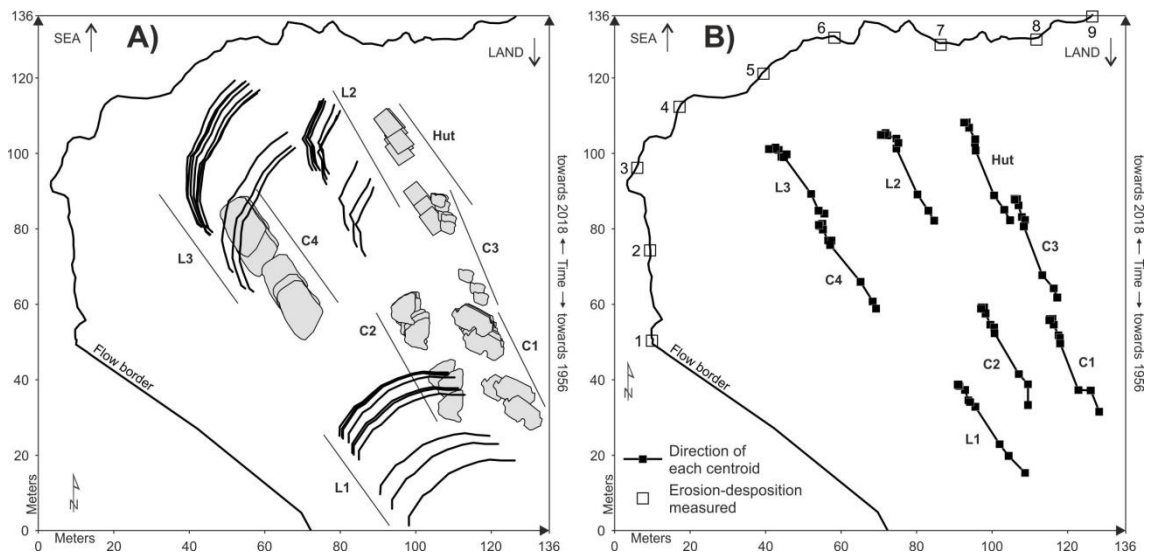


Figure 4. (A) Recorded location, for each of the monitoring periods, of eight features on the flow from 1956 to 2018. They include 4 large boulders (clasts C1 to C4), 3 topographic lobes (L1 to L3), and the foundations of a former hut. The labeled straight lines show the total distance traveled by each feature over the study period. (B) Corresponding changes in the location of the centroids and the transport paths of the eight tracked features. The sites (1 to 9 only, 10 is further east) used to record wave erosion are shown along the coast.



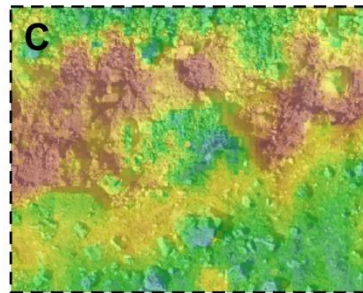
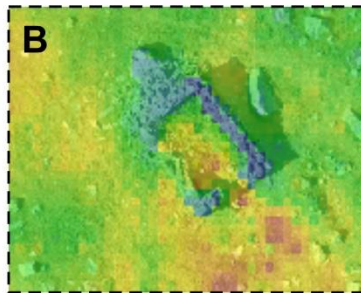
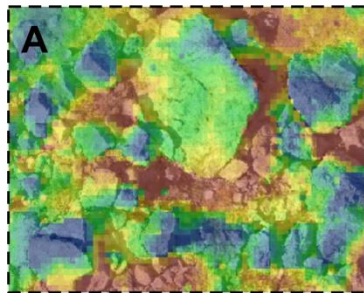
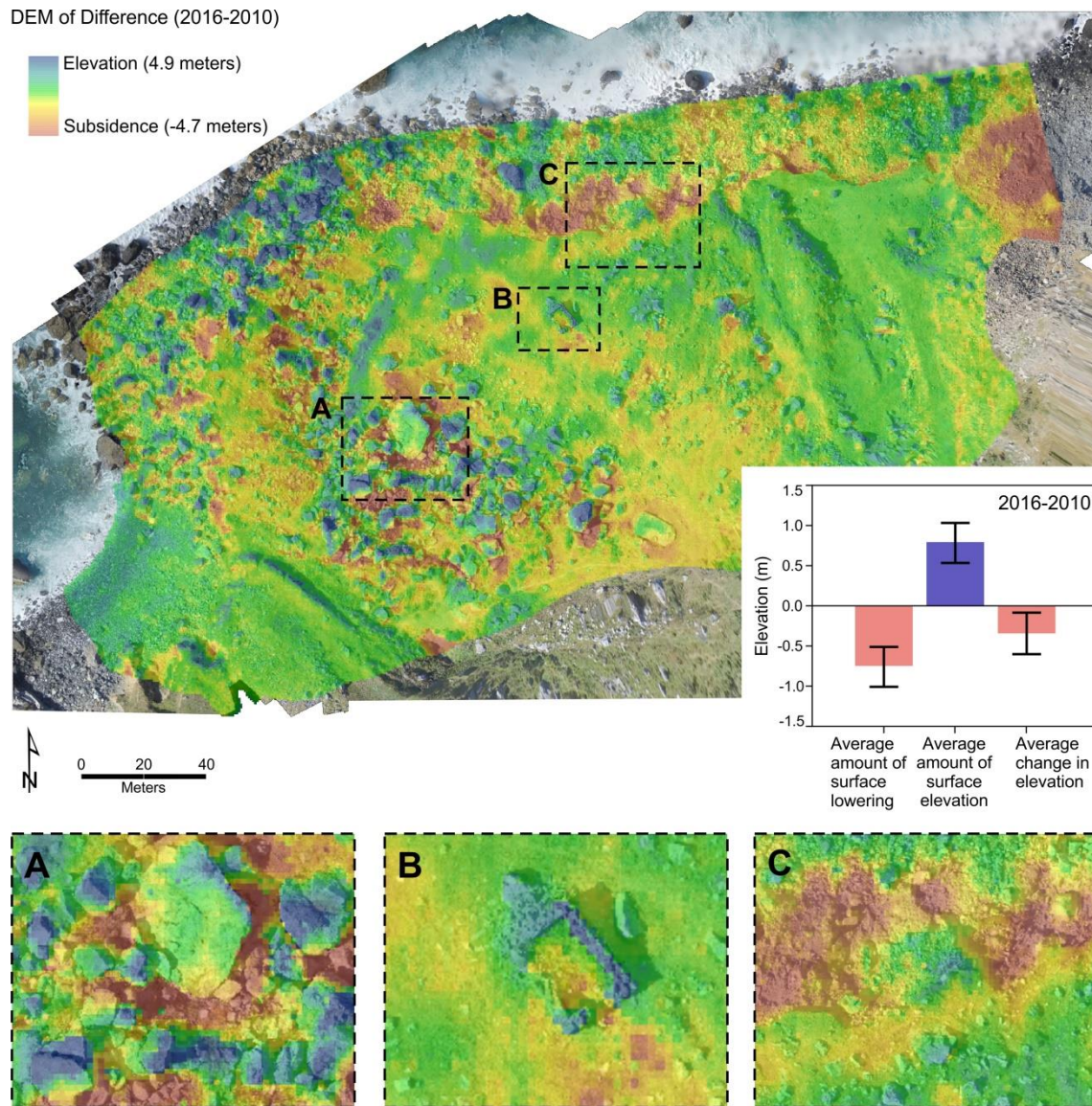


Figure 5. DEM of difference showing changes in the surface elevation of the flow between 2010 and 2016. A, B, and C provide more detailed information from three sample areas, with summary statistics illustrated in the accompany bar graph.

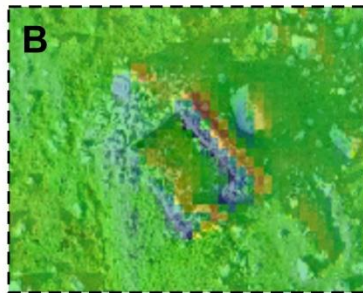
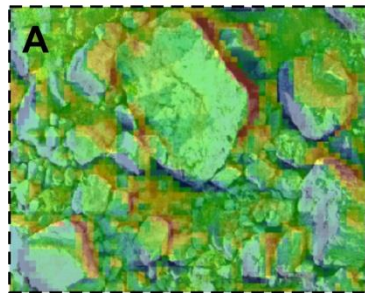
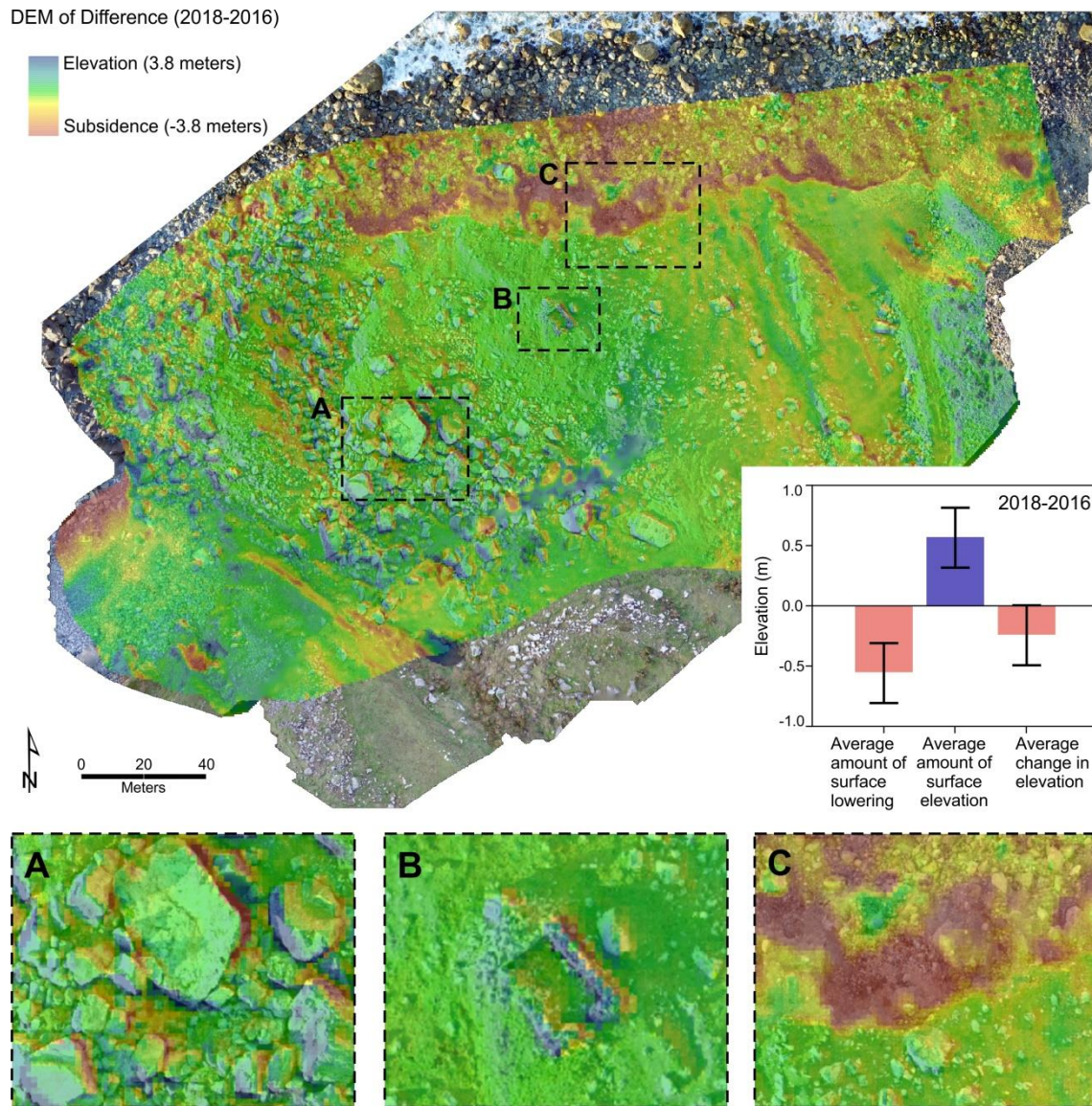


Figure 6. DEM of difference showing changes in the surface elevation of the flow between 2016 and 2018. A, B, and C provide more detailed information from three sample areas, with summary statistics illustrated in the accompany bar graph.



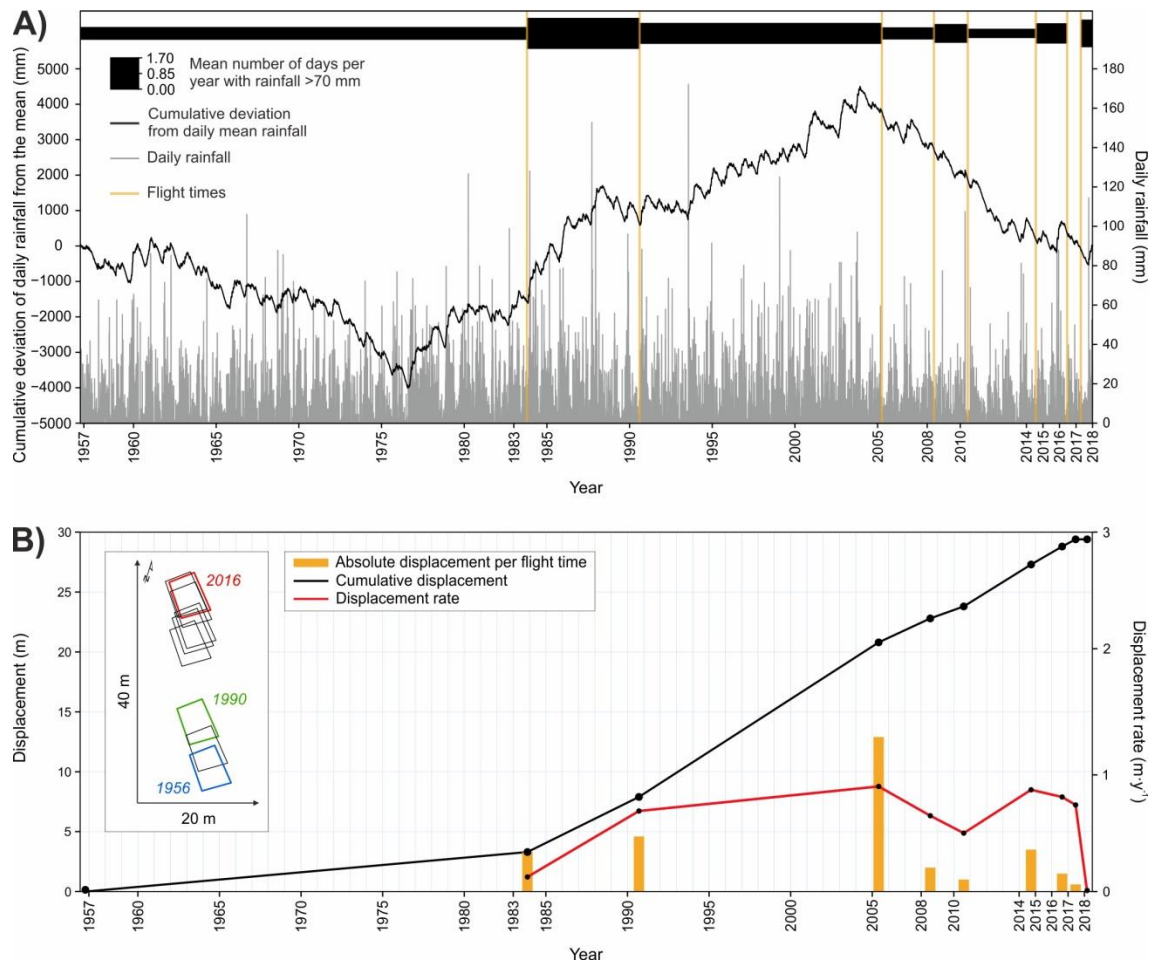


Figure 7. (A) Daily rainfall and cumulative deviation of daily precipitation from the mean. (B) Earthflow movement over the study period based on the location of the hut which, in contrast to other parts of the flow, did not move from 2017 to 2018.

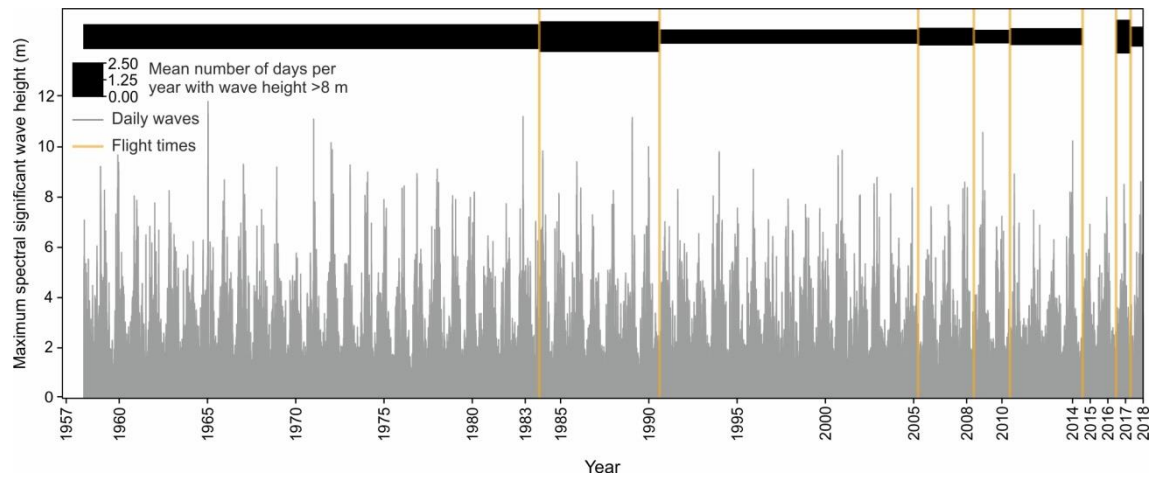


Figure 8. Maximum spectral significant wave height and the number of days with maximum wave heights > 8 m.

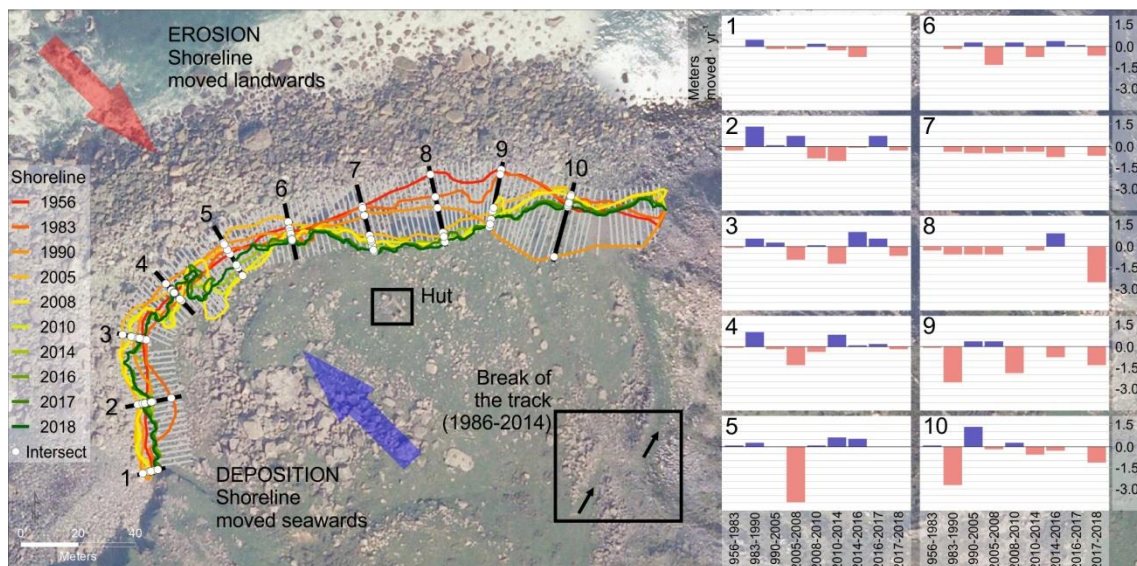


Figure 9. Mapped and graphed changes in the location of the coast at each of the 10 points (lines) located approximately 24 m apart along the toe of the flow. The break in the road refers to movement of a path (from 1986 to 2018) constructed in order to remove the ship wreck.



Figure 10. The 1986 wreck of the 185 m-long freighter Bonnie Carrier, showing the track and other modifications made to the valley to provide access and to expedite its removal. The images on the left were scanned from Concello de Cariño (2010), and the ones on the right from San Claudio Santa Cruz (1997).

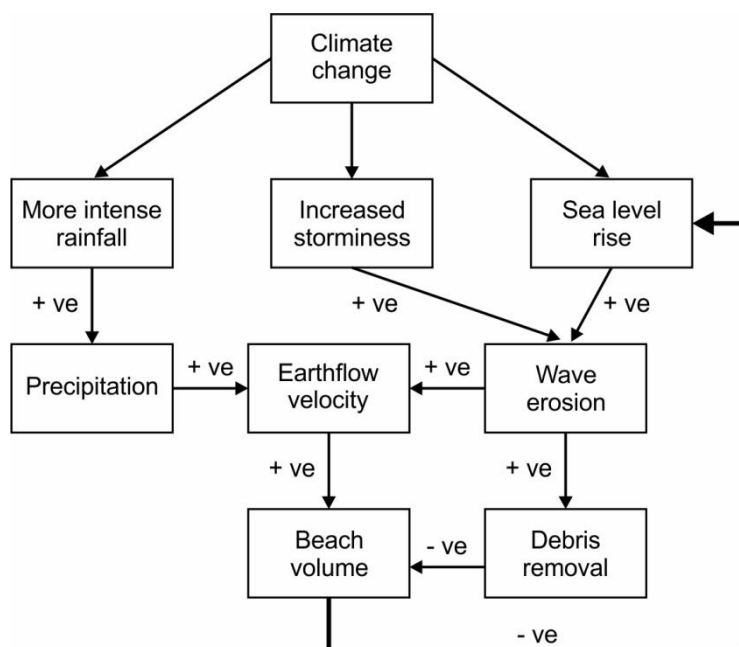


Figure 11. Possible relationships between earthflow activity and a variety of terrestrial and marine conditions. The thick line represents the negative feedback effect of earthflow velocity, and consequently beach height and volume, on wave erosional efficacy.